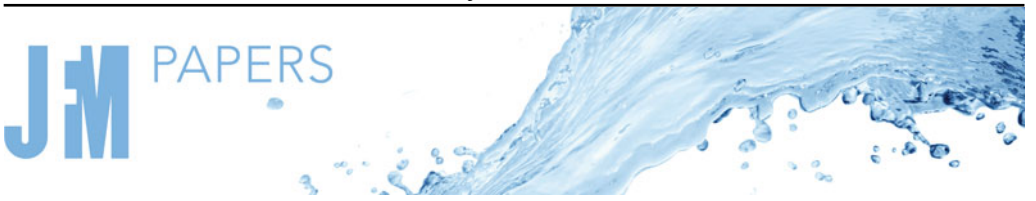
J. Fluid Mech. (2026), *vol.* 1030, A44, doi:10.1017/jfm.2026.11268



Statistical integro-differential fracture model (Sid-FM) for homogenised scalar transport

Shangyi Cao[1], **Daniel Stalder**[1], **Daniel W. Meyer**[1] **and Patrick Jenny**[1]

[1]Institute of Fluid Dynamics, ETH Zürich, Zurich, Switzerland

Corresponding author: Shangyi Cao, shacao@ethz.ch

(Received 2 September 2025; revised 18 December 2025; accepted 2 February 2026)

This work presents an efficient statistical model to simulate expected scalar transport in fractured porous media below the representative elementary volume scale. We focus on embedded, highly conductive, isolated fractures. The statistical integro-differential fracture model (Sid-FM) solves for ensemble-averaged solutions directly, avoiding computationally expensive Monte Carlo simulation. The expected fluid exchange between isolated fractures and the porous matrix is modelled via a non-local kernel function, leading to a set of integro-differential equations. The model is validated against reference data from Monte Carlo simulations for statistically one-dimensional test cases and shows good agreement.

Key words: porous media

1. Introduction

Fractured formations are common in subsurface environments, and they play a crucial role in various applications, including oil and gas reservoirs, geothermal systems and CO_2 storage. Fractures form highly conductive pathways in porous media and significantly influence flow and transport. In the case of sparsely distributed fractures, the representative elementary volume (REV) (Bear 2013) required to measure homogenised properties might be so large that it is in practice impossible to reach (Berre, Doster & Keilegavlen 2019). Practically measurements are taken on a finite volume much smaller than the REV scale. Many models have been proposed for analysing the influence of fractures on flow and transport in porous media based on discrete fracture models, which require detailed and exact knowledge of fractures. Such models include the discrete fracture network method (Cacas *et al.* 1990; Hyman *et al.* 2015) that treats the porous matrix as impermeable,

© The Author(s), 2026. Published by Cambridge University Press. This is an Open Access article, distributed under the terms of the Creative Commons Attribution licence (https://creativecommons.org/licenses/by/4.0/), which permits unrestricted re-use, distribution and reproduction, provided the original article is properly cited.

https://doi.org/10.1017/jfm.2026.11268 Published online by Cambridge University Press

and the discrete fracture matrix method (Dietrich *et al.* 2005; Gebauer *et al.* 2002; Neunhäuserer *et al.* 2002; Geiger *et al.* 2004; Reichenberger *et al.* 2006) that incorporates matrix permeability. Alternatively, homogenisation-based models do not resolve fractures explicitly. These include effective permeability models (Oda 1985; Durlofsky 1991), dual-porosity models (Arbogast, Douglas & Hornung 1990) and multi-continua models, typically referred to as multi-rate mass transfer models (Delgoshaie *et al.* 2015). These models are computationally efficient and have few degrees of freedom, which makes them suitable for large-scale simulations. But they tend to produce poor estimates when fractures are not small compared with the domain size (Sen & Ramos 2012; Delgoshaie *et al.* 2015; Chung *et al.* 2018; Berre *et al.* 2019). Alternatively Neuman (1988) proposed a stochastic continuum concept that treats the real measurement as a realisation of a stochastic process on a continuum. This approach does not require the existence of an REV and allows for the extraction of homogenised properties from a finite volume smaller than an REV. The method relies on Monte Carlo simulations (MCS) to generate a large number of realisations, which are then ensemble averaged to obtain homogenised properties (Cacas *et al.* 1990; Paleologos 2003; Lee, Lough & Jensen 2001; Min, Jing & Stephansson 2004). The MCS approach is computationally expensive, especially for large domains or complex fracture networks.

In our previous work (Jenny 2020; Stalder *et al.* 2025; Cao *et al.* 2025), we proposed a model that solves for ensemble-averaged pressure profiles and flow rates directly from given fracture statistics, circumventing the need for MCS. The model incorporates matrix permeability and therefore accounts for the non-local fluid exchange between embedded, highly conductive, isolated or weakly connected fractures and the porous matrix. The non-local interaction is described by kernel functions, which leads to a set of integro-differential equations and provides accurate estimates of the expected flow rates and pressure distributions in fractured porous media at sub-REV scales as well as at REV scales. The kernel formulation lies at the core of our model. It expresses the expected fluid exchange as a linear function of the pressure difference between the fracture point $\boldsymbol{x}$ and the matrix point $\boldsymbol{x}'$, with the proportionality coefficient given by a kernel function. In previous work, we used top-hat functions as kernels, that is,

$$\hat{g}(\boldsymbol{x}, \boldsymbol{x}') = \begin{cases} \bar{g}, & \text{if } (\boldsymbol{x}' - \boldsymbol{x}) \in \hat{\Omega}_{support}, \\ 0, & \text{otherwise}, \end{cases} \tag{1.1}$$

where the kernel amplitude represents the interaction strength and the kernel support region reflects fracture length and orientation distributions. The kernel parameters can be estimated from fracture statistics. We reintroduce the kernel concept in this work, but for a more detailed discussion, the reader is referred to Jenny (2020, (2.6), (2.8)–(2.10), (5.1)). For the numerical implementation, the convergence study and the validation of the model, the reader is referred to Stalder *et al.* (2025). In this work, we extend the statistical integro-differential fracture model (Sid-FM) to also describe passive scalar transport in fractured porous media. The model is validated against statistically one-dimensional reference data generated by MCS. The remainder of the paper is structured as follows: § 2 presents the mathematical formulation of the model, § 3 provides a validation of the model using Monte Carlo reference data and § 4 discusses the model's capabilities and limitations, and offers insights into its application for data assimilation.

2. Method

We consider a porous medium domain Ω with embedded, highly conductive, isolated fractures. Viewing the embedded isolated fractures as lower-dimensional manifolds, the

https://doi.org/10.1017/jfm.2026.11268 Published online by Cambridge University Press

mass balance in the matrix of a passive scalar advected by incompressible flow in a control volume δV is given by

$$r_\delta \int_{\delta V} \left.\frac{\partial \phi_m c_m}{\partial t}\right|_{\boldsymbol{x}} \mathrm{d}V(\boldsymbol{x}) + \int_{\partial \delta V} c_m(\boldsymbol{x}) \boldsymbol{u}_m(\boldsymbol{x}) \cdot \boldsymbol{n}(\boldsymbol{x})\, \mathrm{d}A(\boldsymbol{x}) = \int_{\delta V} \sum_{i=1}^{N} \left(c_{f_i}(\boldsymbol{x}) \mathcal{F}_{f_i \to m}(\boldsymbol{x}) - c_m(\boldsymbol{x}) \mathcal{F}_{f_i \leftarrow m}(\boldsymbol{x}) \right) \mathrm{d}V(\boldsymbol{x}), \tag{2.1}$$

where r_δ is the fraction of matrix volume within δV, ϕ_m is the matrix porosity, c_m is the scalar concentration in the matrix, $\boldsymbol{u}_m$ is the flow rate in the matrix, $\boldsymbol{n}$ is the unit normal vector at the control volume boundary $\partial \delta V$ pointing outwards, c_{f_i} is the scalar concentration in fracture f_i, and $\mathcal{F}_{f_i \to m}(\boldsymbol{x})$ and $\mathcal{F}_{f_i \leftarrow m}(\boldsymbol{x})$ are volume flux sources from and to the fracture f_i respectively into and out from the matrix volume δV, which are concentrated on the lower dimensional fracture manifold A_{f_i}. Note that $\mathcal{F}_{f_i \to m}$ and $\mathcal{F}_{f_i \leftarrow m}$ are non-zero only if δV is intersected by the fracture manifold A_{f_i}; N is the total number of fractures in the domain. Also note that by definition $\phi_m(\boldsymbol{x})$ and $c_m(\boldsymbol{x})$ are zero, if $\boldsymbol{x}$ is inside one of the fractures.

For the fractures f_i with their centres $\boldsymbol{x}_{f_i}$ within the control volume δV, the scalar mass balance is given by

$$\begin{aligned} &\int_{\delta V} \sum_{i=1}^{N} \delta(\boldsymbol{x} - \boldsymbol{x}_{f_i}) \int_{A_{f_i}} \left.\frac{\partial a_{f_i} \phi_{f_i} c_{f_i}}{\partial t}\right|_{\boldsymbol{x}'} \mathrm{d}A(\boldsymbol{x}')\mathrm{d}V(\boldsymbol{x}) \\ &= \int_{\delta V} \sum_{i=1}^{N} \delta(\boldsymbol{x} - \boldsymbol{x}_{f_i}) \int_{\Omega} \left(c_m(\boldsymbol{x}') \mathcal{F}_{f_i \leftarrow m}(\boldsymbol{x}') - c_{f_i}(\boldsymbol{x}') \mathcal{F}_{f_i \to m}(\boldsymbol{x}') \right) \mathrm{d}V(\boldsymbol{x}')\mathrm{d}V(\boldsymbol{x}) \\ &+ \int_{\delta V} \sum_{i=1}^{N} \delta(\boldsymbol{x} - \boldsymbol{x}_{f_i}) \int_{\Omega} \left(c_b(\boldsymbol{x}') \mathcal{F}_{f_i \leftarrow b}(\boldsymbol{x}') - c_{f_i}(\boldsymbol{x}') \mathcal{F}_{f_i \to b}(\boldsymbol{x}') \right) \mathrm{d}V(\boldsymbol{x}')\mathrm{d}V(\boldsymbol{x}), \end{aligned} \tag{2.2}$$

where $\delta(\cdot)$ is the Dirac delta function (making sure that only fractures with their centres $\boldsymbol{x}_{f_i}$ inside volume δV contribute), a_{f_i} and ϕ_{f_i} are aperture and porosity of fracture f_i with manifold A_{f_i} and $\mathcal{F}_{b \leftarrow f_i}$ and $\mathcal{F}_{b \to f_i}$ are fluxes to and from the boundary. Note that (2.2) is formulated for the whole fractures with their centres inside δV. Next the stochastic continuum proposed by Neuman (1988) is considered, where the fracture field is a realisation of a probabilistic fracture distribution; note that (2.1) and (2.2) hold for every realisation. For the expected concentration in the matrix one obtains

$$r \int_{\delta V} \frac{\partial \mathbb{E}\left[\phi_m c_m | \boldsymbol{x}\right]}{\partial t} \mathrm{d}V(\boldsymbol{x}) + \int_{\partial \delta V} \mathbb{E}[c_m \boldsymbol{u}_m | \boldsymbol{x}] \cdot \boldsymbol{n}(\boldsymbol{x})\, \mathrm{d}A(\boldsymbol{x}) = \int_{\delta V} \mathbb{E}\left[\sum_{i=1}^{N} (c_{f_i} \mathcal{F}_{f_i \to m} - c_m \mathcal{F}_{f_i \leftarrow m}) \middle| \boldsymbol{x} \right] \mathrm{d}V(\boldsymbol{x}) \tag{2.3}$$

from (2.1), where $r = (1 - \rho_f \overline{V}_f)$ is the expected matrix volume fraction and $\overline{V}_f$ is the mean volume of a single fracture. Here $\mathbb{E}[\cdot|\boldsymbol{x}]$ denotes the expectation at location $\boldsymbol{x}$. It is assumed that the volume fraction r_δ and the concentration $\phi_m c_m$ are not correlated. Using the Gauss theorem, and given that (2.3) needs to hold for any control volume δV, one

https://doi.org/10.1017/jfm.2026.11268 Published online by Cambridge University Press

obtains

$$r\frac{\partial \mathbb{E}\left[\phi_m c_m|\boldsymbol{x}\right]}{\partial t}+\boldsymbol{\nabla}\cdot\mathbb{E}[c_m\boldsymbol{u}_m|\boldsymbol{x}]=\mathbb{E}\left[\sum_{i=1}^{N}(c_{f_i}\mathcal{F}_{f_i\to m}-c_m\mathcal{F}_{f_i\leftarrow m})\middle|\boldsymbol{x}\right] \tag{2.4}$$

for the expected scalar transport in the matrix. Now we approximate

$$\mathbb{E}\left[\sum_{i=1}^{N}\mathcal{F}_{f_i\to m}\middle|\boldsymbol{x}\right]\approx\int_{\Omega\cup\Omega_b}\underbrace{H\left(\bar{p}_f(\boldsymbol{x}')-\bar{p}_m(\boldsymbol{x})\right)\hat{g}(\boldsymbol{x}',\boldsymbol{x})(\bar{p}_f(\boldsymbol{x}')-\bar{p}_m(\boldsymbol{x}))}_{\bar{F}_{f\to m}(\boldsymbol{x}',\boldsymbol{x})}\,\mathrm{d}V(\boldsymbol{x}'), \tag{2.5}$$

$$\mathbb{E}\left[\sum_{i=1}^{N}\mathcal{F}_{f_i\leftarrow m}\middle|\boldsymbol{x}\right]\approx\int_{\Omega\cup\Omega_b}\underbrace{H\left(\bar{p}_m(\boldsymbol{x})-\bar{p}_f(\boldsymbol{x}')\right)\hat{g}(\boldsymbol{x}',\boldsymbol{x})(\bar{p}_m(\boldsymbol{x})-\bar{p}_f(\boldsymbol{x}'))}_{\bar{F}_{f\leftarrow m}(\boldsymbol{x}',\boldsymbol{x})}\,\mathrm{d}V(\boldsymbol{x}'), \tag{2.6}$$

where $H(\cdot)$ is the Heaviside step function and $\bar{p}_f(\boldsymbol{x}')$ and $\bar{p}_m(\boldsymbol{x})$ are the expected pressures of fractures centred at $\boldsymbol{x}'$ and in the matrix at $\boldsymbol{x}$, respectively. Further, the kernel function $\hat{g}(\boldsymbol{x}',\boldsymbol{x})$ from our previous works (Jenny 2020; Stalder *et al.* 2025; Cao *et al.* 2025) is introduced to account for the non-local interaction between fractures $\bar{p}_f(\boldsymbol{x}')$ and matrix $\bar{p}_m(\boldsymbol{x})$. For simplicity, the symbols $\bar{F}_{f\to m}(\boldsymbol{x}',\boldsymbol{x})$ and $\bar{F}_{f\leftarrow m}(\boldsymbol{x}',\boldsymbol{x})$ are introduced, which represent the expected flux density to or from fractures centred at $\boldsymbol{x}'$ to a matrix point $\boldsymbol{x}$. This leads to the approximation

$$\begin{aligned}&\bar{\phi}_m\frac{\partial\bar{c}_m}{\partial t}\bigg|_{\boldsymbol{x}}+\boldsymbol{\nabla}\cdot\mathbb{E}[c_m\boldsymbol{u}_m|\boldsymbol{x}]\\&\approx\int_{\Omega\cup\Omega_b}\bar{c}_f(\boldsymbol{x}')\bar{F}_{f\to m}(\boldsymbol{x}',\boldsymbol{x})-\bar{c}_m(\boldsymbol{x})\bar{F}_{f\leftarrow m}(\boldsymbol{x}',\boldsymbol{x})\,\mathrm{d}V(\boldsymbol{x}')\\&+\int_{\Omega\cup\Omega_b}\mathrm{Cov}[c_f(\boldsymbol{x}'),F_{f\to m}(\boldsymbol{x}',\boldsymbol{x})]-\mathrm{Cov}[c_m(\boldsymbol{x}),F_{f\leftarrow m}(\boldsymbol{x}',\boldsymbol{x})]\,\mathrm{d}V(\boldsymbol{x}'),\end{aligned} \tag{2.7}$$

where $\bar{\phi}_m=(1-\rho_f\overline{V}_f)\phi_m$ is the effective matrix porosity. The covariances $\mathrm{Cov}[\cdot,\cdot]$ are unclosed and require additional modelling assumptions, as is discussed later. Note that $\Omega\cup\Omega_b$ includes the whole domain plus a surrounding layer ensuring that all centres of fractures which intersect with Ω are included, such that fracture/matrix mass exchange is not underestimated close to boundaries (see figure 1). For convenience the notation $\bar{c}_{m,f}(\boldsymbol{x})=\mathbb{E}[c_{m,f}|\boldsymbol{x}]$ has been introduced above and the porosity ϕ_m is assumed to be constant. Further it is assumed that the concentration c_f is constant within a single fracture. For scalar transport through the matrix, Darcy's law is employed and dispersion ignored, that is, the approximation

$$\mathbb{E}[c_m\boldsymbol{u}_m|\boldsymbol{x}]\approx-\left(\bar{c}_m\frac{k}{\mu}\boldsymbol{\nabla}\bar{p}_m\right)_{\boldsymbol{x}} \tag{2.8}$$

is used, where k is the matrix permeability and μ the dynamic viscosity.

https://doi.org/10.1017/jfm.2026.11268 Published online by Cambridge University Press

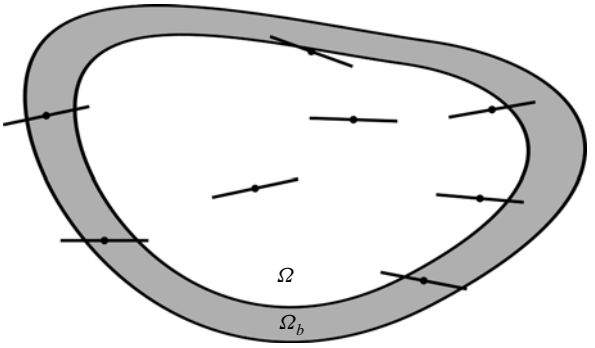


Figure 1. The domain Ω is extended by Ω_b to account for the fractures with their centres out of the boundary but still intersecting the domain.

All together, this leads to the model equation

$$\begin{aligned}&\bar{\phi}_m \frac{\partial \bar{c}_m}{\partial t}\bigg|_{\boldsymbol{x}} - \nabla \cdot \left(\bar{c}_m \frac{k}{\mu} \nabla \bar{p}_m\right)_{\boldsymbol{x}} \\ &= \int_{\Omega \cup \Omega_b} \bar{c}_f(\boldsymbol{x}') \bar{F}_{f \to m}(\boldsymbol{x}', \boldsymbol{x}) + \mathrm{Cov}[c_f(\boldsymbol{x}'), F_{f \to m}(\boldsymbol{x}', \boldsymbol{x})] \, \mathrm{d}V(\boldsymbol{x}') \\ &- \int_{\Omega \cup \Omega_b} \bar{c}_m(\boldsymbol{x}) \bar{F}_{f \leftarrow m}(\boldsymbol{x}', \boldsymbol{x}) + \mathrm{Cov}[c_m(\boldsymbol{x}), F_{f \leftarrow m}(\boldsymbol{x}', \boldsymbol{x})] \, \mathrm{d}V(\boldsymbol{x}')\end{aligned} \tag{2.9}$$

for $\bar{c}_m$. Similarly, from (2.2) one obtains the equation

$$\begin{aligned}&\frac{\partial}{\partial t} \mathbb{E}\left[\sum_{i=1}^{N} \left(\delta(\boldsymbol{x} - \boldsymbol{x}_{f_i}) \int_{A_{f_i}} a_{f_i}(\boldsymbol{x}') \phi_{f_i} c_{f_i}(\boldsymbol{x}') \, \mathrm{d}A(\boldsymbol{x}')\right) \bigg| \boldsymbol{x}\right] \\ &= \mathbb{E}\left[\sum_{i=1}^{N} \left(\delta(\boldsymbol{x} - \boldsymbol{x}_{f_i}) \int_{\Omega} c_m(\boldsymbol{x}') \mathcal{F}_{f_i \leftarrow m}(\boldsymbol{x}') - c_{f_i}(\boldsymbol{x}') \mathcal{F}_{f_i \to m}(\boldsymbol{x}') \, \mathrm{d}V(\boldsymbol{x}')\right) \bigg| \boldsymbol{x}\right] \\ &+ \mathbb{E}\left[\sum_{i=1}^{N} \left(\delta(\boldsymbol{x} - \boldsymbol{x}_{f_i}) \int_{\partial\Omega} c_b(\boldsymbol{x}') \mathcal{F}_{f_i \leftarrow b}(\boldsymbol{x}') - c_{f_i}(\boldsymbol{x}) \mathcal{F}_{f_i \to b}(\boldsymbol{x}) \, \mathrm{d}A(\boldsymbol{x}')\right) \bigg| \boldsymbol{x}\right]\end{aligned} \tag{2.10}$$

for the expected concentration in fractures with centres at $\boldsymbol{x}$. With the assumptions made above, that $\phi_{f_i} = \phi_f = \text{constant}$, and that

$$\mathbb{E}\left[\sum_{i=1}^{N} \left(\delta(\boldsymbol{x} - \boldsymbol{x}_{f_i}) \int_{A_{f_i}} a_{f_i}(\boldsymbol{x}') \phi_{f_i}(\boldsymbol{x}') c_{f_i}(\boldsymbol{x}') \, \mathrm{d}A(\boldsymbol{x}')\right) \bigg| \boldsymbol{x}\right] \approx \underbrace{\rho_f(\boldsymbol{x}) \overline{V}_f \phi_f}_{\bar{\phi}_f \text{(effective fracture porosity)}} \bar{c}_f(\boldsymbol{x}), \tag{2.11}$$

where $\rho_f(\boldsymbol{x})$ is the fracture number density. The boundary fluxes are approximated as

$$\begin{aligned}&\mathbb{E}\left[\sum_{i=1}^{N} \left(\delta(\boldsymbol{x} - \boldsymbol{x}_{f_i}) \int_{\partial\Omega} \mathcal{F}_{f_i \leftarrow b}(\boldsymbol{x}') \, \mathrm{d}A(\boldsymbol{x}')\right) \bigg| \boldsymbol{x}\right] \\ &= \int_{\partial\Omega} \underbrace{H(\bar{p}_b(\boldsymbol{x}') - \bar{p}_f(\boldsymbol{x})) \hat{k}(\boldsymbol{x}, \boldsymbol{x}') \frac{\bar{p}_b(\boldsymbol{x}') - \bar{p}_f(\boldsymbol{x})}{|\boldsymbol{x}' - \boldsymbol{x}|}}_{\bar{F}_{f \leftarrow b}(\boldsymbol{x}, \boldsymbol{x}')} \, \mathrm{d}A(\boldsymbol{x}'),\end{aligned} \tag{2.12}$$

https://doi.org/10.1017/jfm.2026.11268 Published online by Cambridge University Press

$$\mathbb{E}\left[\sum_{i=1}^{N}\left(\delta(\boldsymbol{x}-\boldsymbol{x}_{f_i})\int_{\partial\Omega}\mathcal{F}_{f_i\to b}(\boldsymbol{x})\,\mathrm{d}A(\boldsymbol{x}')\right)\Big|\boldsymbol{x}\right]$$
$$=\int_{\partial\Omega}\underbrace{H(\bar{p}_f(\boldsymbol{x})-\bar{p}_b(\boldsymbol{x}'))\hat{k}(\boldsymbol{x},\boldsymbol{x}')\frac{\bar{p}_f(\boldsymbol{x})-\bar{p}_b(\boldsymbol{x}')}{|\boldsymbol{x}'-\boldsymbol{x}|}}_{\bar{F}_{f\to b}(\boldsymbol{x},\boldsymbol{x}')}\,\mathrm{d}A(\boldsymbol{x}'),\tag{2.13}$$

where the boundary kernel function $\hat{k}(\boldsymbol{x},\boldsymbol{x}')$ from our previous work (Jenny 2020; Stalder *et al.* 2025; Cao *et al.* 2025) is applied, which accounts for the flow from a boundary point $\boldsymbol{x}'$ through the fracture to its centre located at $\boldsymbol{x}$. The symbols $\bar{F}_{f\leftarrow b}(\boldsymbol{x},\boldsymbol{x}')$ and $\bar{F}_{f\to b}(\boldsymbol{x},\boldsymbol{x}')$ are introduced for convenience, which represent expected flux densities from and to the boundary at $\boldsymbol{x}'$ to fractures centred at $\boldsymbol{x}$. This leads to the approximation

$$\begin{aligned}\bar{\phi}_f\frac{\partial\bar{c}_f}{\partial t}\bigg|_{\boldsymbol{x}}\approx&\int_\Omega\bar{c}_m(\boldsymbol{x}')\bar{F}_{f\leftarrow m}(\boldsymbol{x},\boldsymbol{x}')+\mathrm{Cov}\left[c_m(\boldsymbol{x}'),\,F_{f\leftarrow m}(\boldsymbol{x},\boldsymbol{x}')\right]\,\mathrm{d}V(\boldsymbol{x}')\\&-\int_\Omega\bar{c}_f(\boldsymbol{x})\bar{F}_{f\to m}(\boldsymbol{x},\boldsymbol{x}')+\mathrm{Cov}\left[c_f(\boldsymbol{x}),\,F_{f\to m}(\boldsymbol{x},\boldsymbol{x}')\right]\,\mathrm{d}V(\boldsymbol{x}')\\&+\int_{\partial\Omega}\bar{c}_b(\boldsymbol{x}')\bar{F}_{f\leftarrow b}(\boldsymbol{x},\boldsymbol{x}')+\mathrm{Cov}[c_b(\boldsymbol{x}'),\,F_{f\leftarrow b}(\boldsymbol{x},\boldsymbol{x}')]\,\mathrm{d}A(\boldsymbol{x}')\\&-\int_{\partial\Omega}\bar{c}_f(\boldsymbol{x})\bar{F}_{f\to b}(\boldsymbol{x},\boldsymbol{x}')+\mathrm{Cov}[c_f(\boldsymbol{x}'),\,F_{f\to b}(\boldsymbol{x},\boldsymbol{x}')]\,\mathrm{d}A(\boldsymbol{x}').\end{aligned}\tag{2.14}$$

As in Jenny (2020), $\hat{g}(\boldsymbol{x},\boldsymbol{x}')$ and $\hat{k}(\boldsymbol{x},\boldsymbol{x}')$ are described by top hat functions, that is,

$$\hat{g}(\boldsymbol{x},\boldsymbol{x}')=\begin{cases}\bar{g} & \text{if } (\boldsymbol{x}'-\boldsymbol{x})\in\hat{\Omega}_{support},\\ 0 & \text{else}\end{cases}\tag{2.15}$$

and

$$\hat{k}(\boldsymbol{x},\boldsymbol{x}')=\begin{cases}\bar{k} & \text{if } (\boldsymbol{x}'-\boldsymbol{x})\in\hat{\Omega}_{support},\\ 0 & \text{else.}\end{cases}\tag{2.16}$$

The kernel support region $\hat{\Omega}_{support}$ reflects fracture length and orientation distributions; in one dimension it has been chosen to be $\hat{\Omega}_{support}=[-l_f/2,\,l_f/2]$, where l_f is the maximum fracture length. A more detailed discussion of the kernel functions can be found in Appendix A. Note that, provided $\hat{g}$ and $\hat{k}$ are known, all terms in (2.9) and (2.14) are closed, except for the covariances. Here we assume that in a single realisation diffusion is negligible and thus $c_m,\,c_f\in\{0,\,1\}$; in other words, c_m and c_f are Bernoulli random variables. In that case we can write for c representing c_m or c_f

$$\mathrm{Cov}[c,\,F]=\bar{c}\mathbb{E}[F|c=1]-\bar{c}\mathbb{E}[F]=\underbrace{\bar{c}(1-\bar{c})}_{\mathrm{Var}(c)}\left(\mathbb{E}[F|c=1]-\mathbb{E}[F|c=0]\right).\tag{2.17}$$

In the presence of a fracture, the flow near the fracture is dominated by the matrix–fracture fluid exchange. We estimate the flow u to be proportional to the flux density F, that is, $u\propto F$. When a concentration front is at a distance Δx from a fracture, then the probability that the front reaches that fracture after time Δt is given by $P(c=1)=P(u>\Delta x/\Delta t)=P(F>F_0)$ for some fixed value F_0. We assume that the flux density F is symmetric and bounded around its mean $\mathbb{E}[F]$. For simplicity, we further assume that F is uniformly

https://doi.org/10.1017/jfm.2026.11268 Published online by Cambridge University Press

distributed, i.e. $F \sim U((1-\alpha)\mathbb{E}[F], (1+\alpha)\mathbb{E}[F])$ for some $\alpha > 0$. Then one obtains

$$\mathbb{E}[F|c=1] = \mathbb{E}[F|F > F_0] = \frac{(1+\alpha)\mathbb{E}[F] + F_0}{2}, \tag{2.18}$$

$$\mathbb{E}[F|c=0] = \mathbb{E}[F|F < F_0] = \frac{(1-\alpha)\mathbb{E}[F] + F_0}{2} \tag{2.19}$$

and

$$\mathbb{E}[F|c=1] - \mathbb{E}[F|c=0] = \alpha\mathbb{E}[F]. \tag{2.20}$$

With this assumption one obtains

$$\mathrm{Cov}[c,\, F] = \bar{c}(1-\bar{c})\alpha\mathbb{E}[F] \tag{2.21}$$

from (2.17), and the modelled equations for $\bar{c}_m$ and $\bar{c}_f$ become

$$\begin{aligned}\bar{\phi}_m \frac{\partial \bar{c}_m}{\partial t}\bigg|_{\boldsymbol{x}} - \boldsymbol{\nabla}\cdot\left(\bar{c}_m \frac{k}{\mu}\boldsymbol{\nabla}\bar{p}_m\right)_{\boldsymbol{x}} \approx{}& \int_{\Omega\cup\Omega_b} \bar{c}_f(\boldsymbol{x}')\left(1+\alpha(1-\bar{c}_f(\boldsymbol{x}'))\right)\bar{F}_{f\to m}(\boldsymbol{x}',\boldsymbol{x})\,\mathrm{d}V(\boldsymbol{x}') \\ &- \int_{\Omega\cup\Omega_b} \bar{c}_m(\boldsymbol{x})\left(1+\alpha(1-\bar{c}_m(\boldsymbol{x}))\right)\bar{F}_{f\leftarrow m}(\boldsymbol{x}',\boldsymbol{x})\,\mathrm{d}V(\boldsymbol{x}')\end{aligned} \tag{2.22}$$

and

$$\begin{aligned}\bar{\phi}_f \frac{\partial \bar{c}_f}{\partial t}\bigg|_{\boldsymbol{x}} \approx{}& \int_{\Omega} \bar{c}_m(\boldsymbol{x}')\left(1+\alpha(1-\bar{c}_m(\boldsymbol{x}'))\right)\bar{F}_{f\leftarrow m}(\boldsymbol{x},\boldsymbol{x}')\,\mathrm{d}V(\boldsymbol{x}') \\ &- \int_{\Omega} \bar{c}_f(\boldsymbol{x})\left(1+\alpha(1-\bar{c}_f(\boldsymbol{x}))\right)\bar{F}_{f\to m}(\boldsymbol{x},\boldsymbol{x}')\,\mathrm{d}V(\boldsymbol{x}') \\ &+ \int_{\partial\Omega} \bar{c}_b(\boldsymbol{x}')\left(1+\alpha(1-\bar{c}_b(\boldsymbol{x}'))\right)\bar{F}_{f\leftarrow b}(\boldsymbol{x},\boldsymbol{x}')\,\mathrm{d}A(\boldsymbol{x}') \\ &- \int_{\partial\Omega} \bar{c}_f(\boldsymbol{x})\left(1+\alpha(1-\bar{c}_f(\boldsymbol{x}))\right)\bar{F}_{f\to b}(\boldsymbol{x},\boldsymbol{x}')\,\mathrm{d}A(\boldsymbol{x}'),\end{aligned} \tag{2.23}$$

respectively.

That (2.22) and (2.23) are consistent with the flow equations in Jenny (2020) can be seen if one sets $\bar{c}_m = \bar{c}_f = 1$, which leads, together with the definitions from (2.5) and (2.6), to

$$\begin{aligned}0 &= \int_{\Omega\cup\Omega_b} \bar{F}_{f\to m}(\boldsymbol{x}',\boldsymbol{x}) - \bar{F}_{f\leftarrow m}(\boldsymbol{x}',\boldsymbol{x})\,\mathrm{d}V(\boldsymbol{x}') + \boldsymbol{\nabla}\cdot\left(\frac{k}{\mu}\boldsymbol{\nabla}\bar{p}_m\right)_{\boldsymbol{x}} \\ &= \int_{\Omega\cup\Omega_b} \hat{g}(\boldsymbol{x}',\boldsymbol{x})\left(\bar{p}_f(\boldsymbol{x}') - \bar{p}_m(\boldsymbol{x})\right)\,\mathrm{d}V(\boldsymbol{x}') + \boldsymbol{\nabla}\cdot\left(\frac{k}{\mu}\boldsymbol{\nabla}\bar{p}_m\right)_{\boldsymbol{x}},\end{aligned} \tag{2.24}$$

and further with the definitions from (2.12) and (2.13) to

$$\begin{aligned}0 &= \int_{\Omega} \bar{F}_{f\leftarrow m}(\boldsymbol{x},\boldsymbol{x}') - \bar{F}_{f\to m}(\boldsymbol{x},\boldsymbol{x}')\,\mathrm{d}V(\boldsymbol{x}') + \int_{\partial\Omega} \bar{F}_{f\leftarrow b}(\boldsymbol{x},\boldsymbol{x}') - \bar{F}_{f\to b}(\boldsymbol{x},\boldsymbol{x}')\,\mathrm{d}A(\boldsymbol{x}') \\ &= \int_{\Omega} \hat{g}(\boldsymbol{x},\boldsymbol{x}')\left(\bar{p}_m(\boldsymbol{x}') - \bar{p}_f(\boldsymbol{x})\right)\,\mathrm{d}V(\boldsymbol{x}') + \int_{\partial\Omega} \hat{k}(\boldsymbol{x},\boldsymbol{x}')\frac{\bar{p}_b(\boldsymbol{x}') - \bar{p}_f(\boldsymbol{x})}{|\boldsymbol{x}'-\boldsymbol{x}|}\,\mathrm{d}A(\boldsymbol{x}'),\end{aligned} \tag{2.25}$$

which, as demonstrated in Jenny (2020), are able to accurately predict $\bar{p}_m$ and $\bar{p}_f$ profiles, as well as flow rates through fractures and matrix. The reader is referred to Jenny (2020) for more details on the coupling between the expected flow rate and the expected pressure.

https://doi.org/10.1017/jfm.2026.11268 Published online by Cambridge University Press

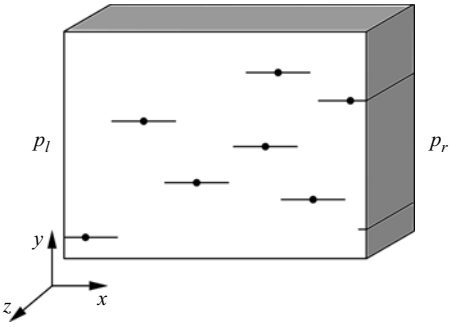


Figure 2. Illustration of the fractured domain (one realisation) (Cao *et al.* 2025). The domain size is $L_x \times L_y = 1.0 \times 0.5$ and all fractures are aligned with the x direction. The left and right boundary pressures are $p_l = 1.0$ and $p_r = 0.0$, respectively; periodic boundary conditions are imposed in the y direction. The initial concentration is zero in the whole domain.

3. Results

The model is validated against reference data generated from MCS. Figure 2 shows the general set-up for all test cases. The domain size is $L_x \times L_y = 1.0 \times 0.5$. A mean pressure gradient is imposed in the x direction between the left and right boundaries. The left boundary pressure is $p_l = 1$ and the right boundary pressure is $p_r = 0$. Periodic boundary conditions are imposed in the y direction, such that in all test cases the fracture distributions are statistically one-dimensional. As initial condition a concentration front with $c = 1$ is imposed at the left boundary, while inside the domain the initial concentration is zero. Fractures are aligned along the x direction. The porosity of the matrix is $\phi_m = 0.1$, the porosity of the fractures is $\phi_f = 1$, the matrix permeability is $k_m = 1$ and the fracture permeability is $k_f = 10^5$. In all test cases the fracture aspect ratio, i.e. the ratio l_f/a_f of fracture length to fracture aperture, is set to 10^3. For each test case a MCS reference with 1000 fracture field realisations is used. First, the expected flow equations (2.24) and (2.25) are solved as described in Jenny (2020). In particular, a finite-volume scheme was used, where the fractures are upscaled to the grid cells they intersect (Kasap & Lake 1990). For solving the linear system, a direct solver (Li *et al.* 1999) was employed. With the obtained flow solution the expected transport equations (2.22) and (2.23) are solved with a forward Euler scheme. To obtain the Monte Carlo reference, a second-order finite-volume scheme was employed. The same time step size and grid resolution, i.e. $\Delta t = 5 \times 10^{-7}$ and $\Delta x = \Delta y = 0.01$, were chosen for both the MCS and the Sid-FM transport calculations. The constant α in (2.21) was set to 0.5 for all test cases. The kernel amplitude $\bar{g}$ was obtained from the scaling law proposed in Cao *et al.* (2025), except for test case 2, where the kernel amplitude was derived from MCS on very large periodic domains (Jenny 2020; Stalder *et al.* 2025). For all figures in the following, the solid lines represent model predictions, while the dotted lines depict MCS reference data. The three columns correspond to three different times, $t = 0.005$, $t = 0.015$ and $t = 0.045$ (left-hand, middle and right-hand columns, respectively). The averaged scalar concentrations in the matrix and fracture domains along the x direction are plotted in the top and bottom rows, respectively.

3.1. *Test case 1: homogeneous fracture statistics with uniform fracture lengths*

In this test case, fractures with uniform length $l_f = 0.25$ are sampled and spatially uniformly distributed in the domain, while the fracture number density is $\rho_f = 50.0$. Figure 3 shows the comparison between model prediction and the MCS reference data.

https://doi.org/10.1017/jfm.2026.11268 Published online by Cambridge University Press

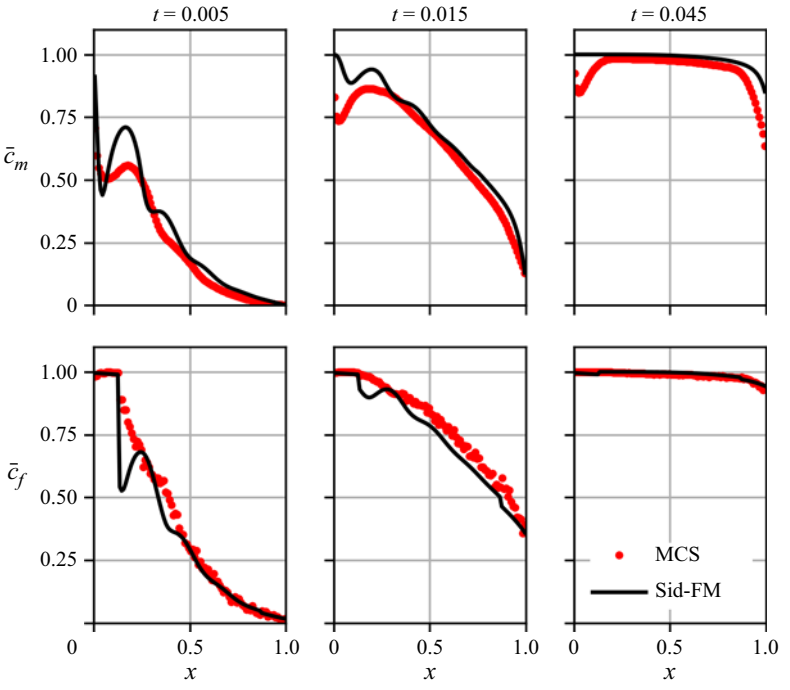


Figure 3. Test case 1. Comparison of scalar concentration along the x direction between model predictions and MCS reference data. Fractures have a uniform length of $l_f = 0.25$ and the fracture number density is $\rho_f = 50$. The three columns correspond to the three different times $t = 0.005$, $t = 0.015$ and $t = 0.045$ (left-hand, middle and right-hand columns, respectively). The solid lines depict model predictions and the circles MCS reference data.

3.2. *Test case 2: homogeneous fracture statistics with power-law-distributed fracture lengths*

In this test case, fractures with power-law-distributed length l_f are sampled and spatially uniformly distributed in the domain. The power-law distribution is given by

$$\rho_f = 0.1 l_f^{-2} \quad \text{for } l_f \in [0.1, 0.5]. \tag{3.1}$$

In this case the kernels given in (2.15) and (2.16) need to be modified according to Stalder *et al.* (2025). Figure 4 shows the comparison between the model prediction and the reference data from MCS.

3.3. *Test case 3: heterogeneous fracture statistics with discontinuously varying fracture lengths*

In this test case, the length of the fractures changes discontinuously at the middle of the domain. The left half of the domain contains fractures of length $l_f = 0.11$ and in the right half of the domain the fractures have a length of $l_f = 0.21$. The fracture number density is $\rho_f = 30.0$ in the whole domain. Figure 5 shows the comparison between the model prediction and the MCS reference data.

https://doi.org/10.1017/jfm.2026.11268 Published online by Cambridge University Press

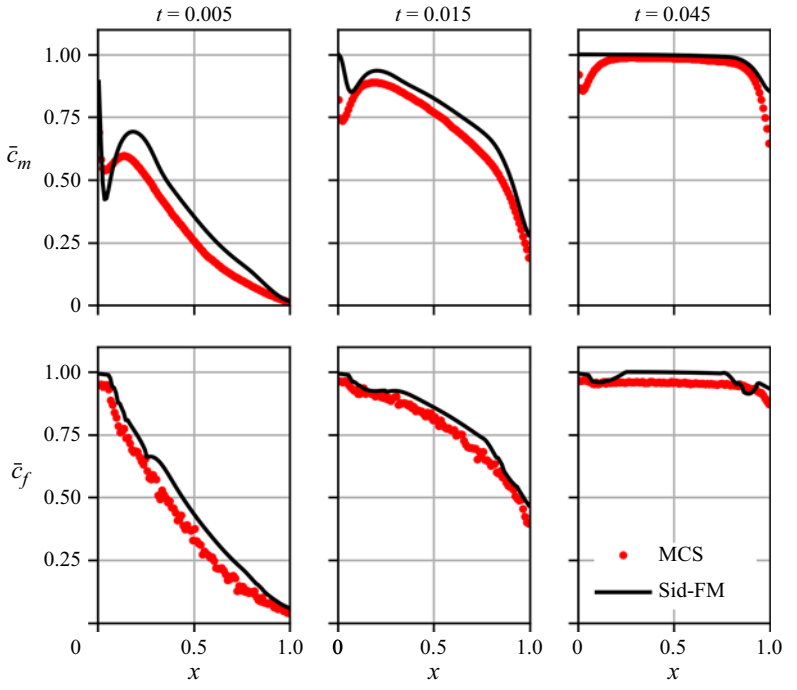


Figure 4. Test case 2. Comparison of scalar concentration along the x direction between model predictions and MCS reference data. Fractures have a power-law-distributed number density $\rho_f = 0.1 l_f^{-2}$, and the fracture length is $l_f \in [0.1, 0.5]$ in the whole domain. The three columns correspond to the three different times $t = 0.005$, $t = 0.015$ and $t = 0.045$ (left-hand, middle and right-hand columns, respectively). The solid lines depict model predictions and the circles MCS reference data.

3.4. *Test case 4: heterogeneous fracture statistics with discontinuously varying fracture number density*

In this test case, the fracture number density changes discontinuously at the middle of the domain. The fracture number density is $\rho_f = 10.0$ in the left half of the domain and $\rho_f = 50.0$ in the right half of the domain. The fracture length is $l_f = 0.25$ in the whole domain. Figure 6 shows the comparison between model predictions and the MCS reference data.

3.5. *Test case 5: heterogeneous fracture statistics with continuously varying fracture length*

In this test case, the length of the fractures changes linearly from $l_f = 0.11$ at the left boundary to $l_f = 0.51$ at the right boundary, and the fracture number density is $\rho_f = 30.0$ across the whole domain. Figure 7 shows comparisons between model predictions and the MCS reference data.

3.6. *Test case 6: heterogeneous fracture statistics with continuously varying fracture number density*

In this test case, the fracture number density changes linearly from $\rho_f = 10.0$ at the left boundary to $\rho_f = 60.0$ at the right boundary, and the fracture length is $l_f = 0.25$ across the whole domain. Figure 8 shows the comparison between model predictions and the MCS reference data.

https://doi.org/10.1017/jfm.2026.11268 Published online by Cambridge University Press

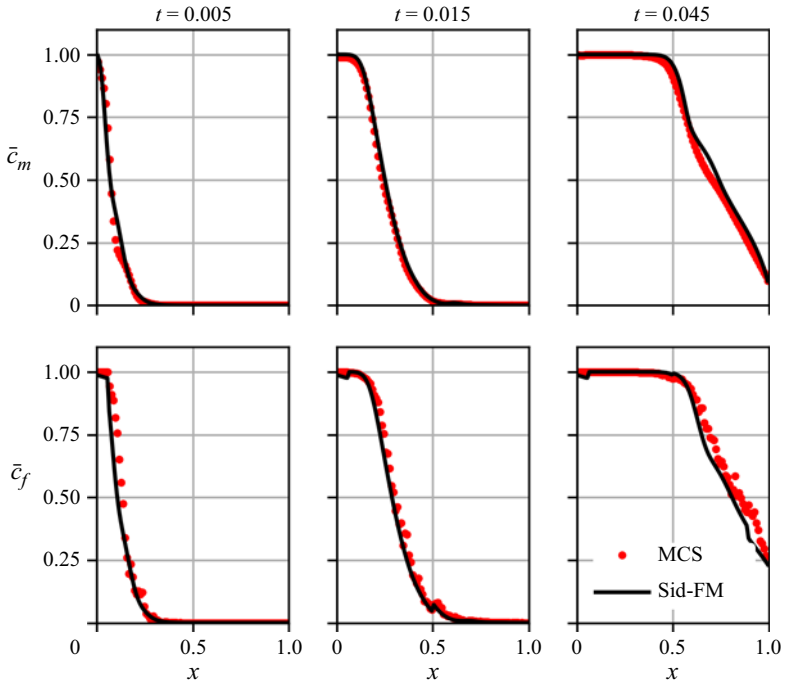


Figure 5. Test case 3. Comparison of scalar concentration along the x direction between model predictions and MCS reference data. The left half of the domain contains fractures of length $l_f = 0.11$ and the right half fractures of length $l_f = 0.21$, and the fracture number density is $\rho_f = 30.0$ in the whole domain. The three columns correspond to the three different times $t = 0.005$, $t = 0.015$ and $t = 0.045$ (left-hand, middle and right-hand columns, respectively). The solid lines depict model predictions and the circles MCS reference data.

4. Discussion and conclusions

In this work, we have extended the Sid-FM proposed by Jenny (2020) to simulate passive scalar transport. Numerical studies of statistically one-dimensional test cases with both homogeneous and heterogeneous fracture statistics have shown good agreement with the MCS reference data. The model is capable of capturing the non-local interactions between fractures and matrix, thus allowing for efficient simulations of scalar transport processes below the REV scale. In contrast to the flow problem discussed in previous works (Jenny 2020; Stalder *et al.* 2025; Cao *et al.* 2025), scalar transport involves covariance terms, which we closed with an algebraic model only depending on the expected quantities computed by the model, and an empirical constant. The good agreement between the model result and MCS reference data shows that the non-local fracture–matrix interaction, represented by the model, is a necessary key mechanism to properly capture the flow and transport processes in the sub-REV regime. The oscillations in the spatial distributions of the presented method exaggerate the phenomena observed in some of the MCS data; they likely stem from the following sources:

(i) assigning a constant concentration within each fracture,
(ii) neglecting dispersion in the matrix.

The first assumption is fundamental to the model formulation, while the second assumption can be relaxed by incorporating dispersion in the matrix, as discussed below.

https://doi.org/10.1017/jfm.2026.11268 Published online by Cambridge University Press

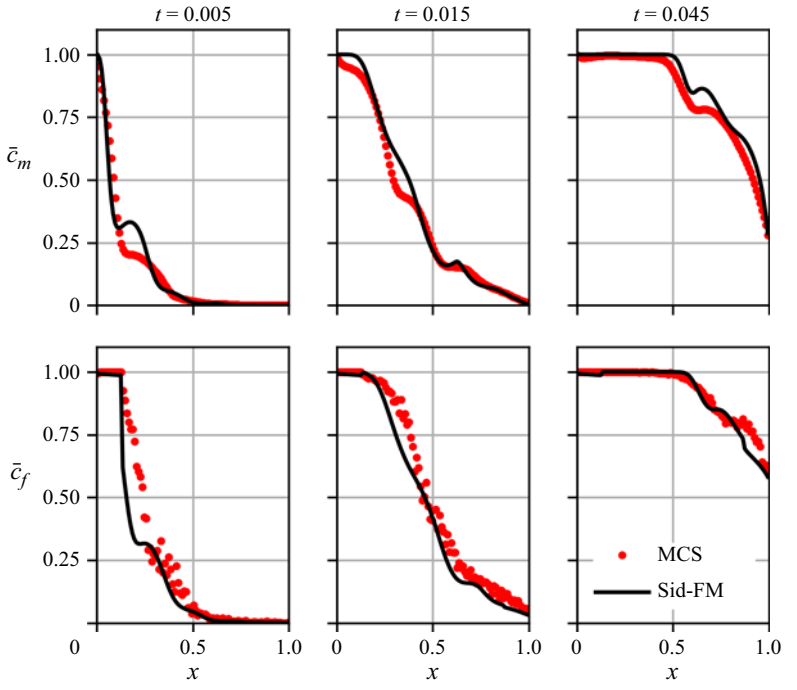


Figure 6. Test case 4. Comparison of scalar concentration along the x direction between model predictions and MCS reference data. The fracture number density is $\rho_f = 10.0$ in the left half of the domain and $\rho_f = 50.0$ in the right half of the domain, and the fracture length is $l_f = 0.25$ in the whole domain. The three columns correspond to the three different times $t = 0.005$, $t = 0.015$ and $t = 0.045$ (left-hand, middle and right-hand columns, respectively). The solid lines depict model predictions and the circles MCS reference data.

To provide a fair and transparent assessment of the proposed model at its current stage of development, we outline in the following its limitations and planned future developments. Some limitations are inherent to the model assumptions, others require further investigation and some are conceptually understood, but not implemented.

(i) The model equations and the closure ansatz are formulated for expected quantities. Thus, the model cannot provide any information about higher-order statistics, such as variances of pressure or concentration fields. However, the low cost of the model makes it attractive for data assimilation. In discrete fracture models, to match sparse measurement data, hydraulic aperture (Snow 1965), fracture orientations (Snow 1969) and fracture number density may be tuned, depending on the available information. Often the very large number of model parameters allows for good matches, but the level of ambiguity always is large (Neuman 1988). Applying discrete fracture models in data assimilation frameworks requires MCS, which are computationally prohibitive. The proposed model can be used as a surrogate model in such frameworks, allowing for efficient calibration of the model parameters to match sparse measurement data.

(ii) All numerical experiments conducted in this work are statistically one-dimensional and serve as a proof of concept. The model formulation is much more general and applicable to two- and three-dimensional cases. For two- and three-dimensional cases, the kernel functions $\hat{g}$ and $\hat{k}$ need to be constructed appropriately to reflect the underlying fracture statistics. We elaborate more on this point in Appendix A.

https://doi.org/10.1017/jfm.2026.11268 Published online by Cambridge University Press

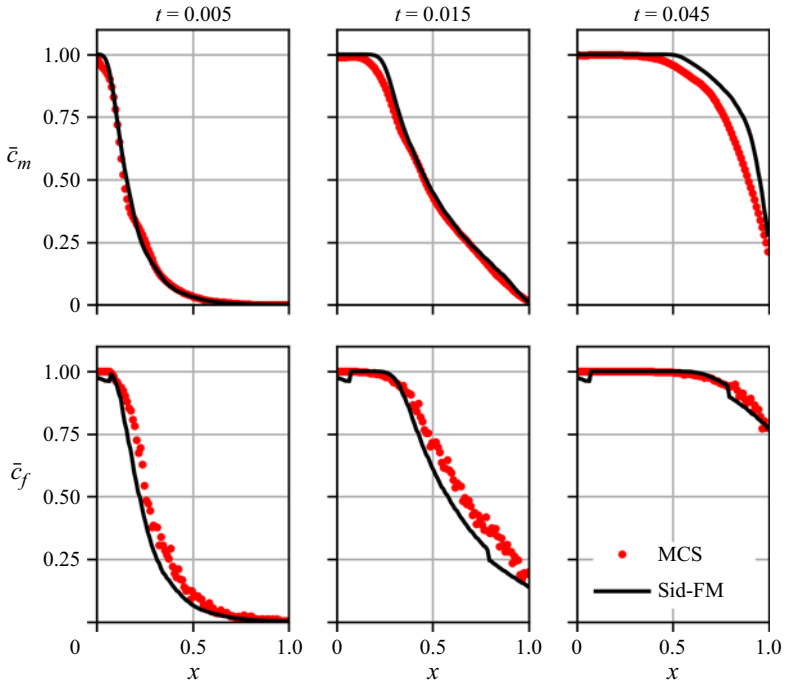


Figure 7. Test case 5. Comparison of scalar concentration along the x direction between model predictions and MCS reference data. The length of the fractures changes linearly from $l_f = 0.11$ at the left boundary to $l_f = 0.51$ at the right boundary, and the fracture number density is $\rho_f = 30.0$ across the whole domain. The three columns correspond to the three different times $t = 0.005$, $t = 0.015$ and $t = 0.045$ (left-hand, middle and right-hand columns, respectively). The solid lines depict model predictions and the circles MCS reference data.

(iii) Intersecting fractures are not explicitly handled in the current framework. In our previous work (Jenny 2020, § 3), it is explained how percolated fracture networks can be incorporated through a local fracture–matrix interaction term. We expect that clusters will behave similarly to isolated fractures, in the sense that their non-local interaction with the matrix can also be represented through a kernel integral, but this is to be investigated.

(iv) We neglected the matrix dispersion term in (2.8). Its effect is most obvious near the domain boundaries. Several formulations would be available to account for it, e.g. classical Fickian dispersion (Dagan 1989) or continuous-time random walk models (Berkowitz *et al.* 2016). Although incorporating these effects for example could be done by incorporating an additional term in the model equations, our results indicate that in the statistically one-dimensional cases dispersion induced by the fractures directly dominates over matrix dispersion. In order to keep the model concise, we opted to omit matrix dispersion while acknowledging that the model could be extended to include it if needed. On the other hand, as in our problem dispersion in the matrix is not due to matrix heterogeneity, but due to fracture-induced streamline curvature, we envision that an adapted kernel formulation could be a promising candidate for modelling matrix dispersion; this is a focus of future work.

(v) The test cases shown in this work are the same as those presented in Jenny (2020), Cao *et al.* (2025) and Stalder *et al.* (2025) for flow problems. These test cases are retained here to provide a direct comparison between flow and transport simulations.

https://doi.org/10.1017/jfm.2026.11268 Published online by Cambridge University Press

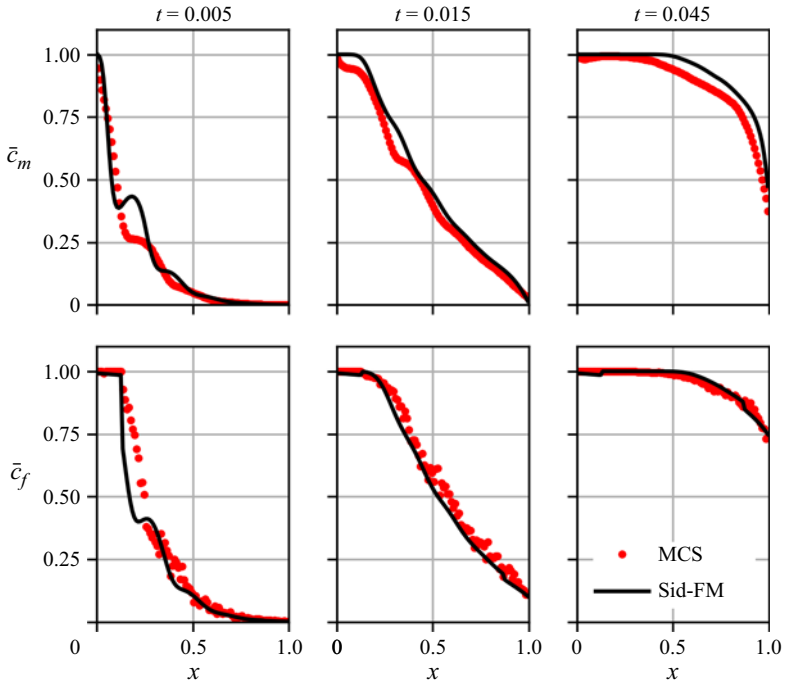


Figure 8. Test case 6. Comparison of scalar concentration along the x direction between model predictions and MCS reference data. The fracture number density changes continuously from $\rho_f = 10.0$ at the left boundary to $\rho_f = 60.0$ at the right boundary, and the fracture length is $l_f = 0.25$ across the whole domain. The three columns correspond to the three different times $t = 0.005$, $t = 0.015$ and $t = 0.045$ (left-hand, middle and right-hand columns, respectively). The solid lines depict model predictions and the circles MCS reference data.

It is expected that the model performance may deteriorate in cases where the fracture statistics exhibit strong discontinuities, such as abrupt changes in fracture number density or length, as the scaling law derived for the kernel amplitude $\bar{g}$ in Cao *et al.* (2025) assumes homogeneous fracture statistics and is applicable to heterogeneous cases only in an approximate sense. Although test cases 3 and 4 represent such scenarios, the model performance remains satisfactory.

Funding. This research received no specific grant from any funding agency, commercial or not-for-profit sectors.

Declaration of interests. The authors report no conflict of interest.

Appendix A. Kernels

Here we demonstrate a way in which one could derive the kernels in two- and three-dimensional problems. As indicated in (2.5), (2.6), (2.12) and (2.13), these kernel functions relate the expected flow exchange between two points in two media as a function of the expected pressure difference. Note that depending on the problem, the arguments of these kernel functions can be points in one-, two- or three-dimensional domains. To keep the discussion concise, we focus here on the $\hat{g}$ kernel. The analysis for the $\hat{k}$ kernel, which governs the expected flow exchange between the fractures and the boundary, proceeds analogously.

https://doi.org/10.1017/jfm.2026.11268 Published online by Cambridge University Press

The expected fluid exchange between fractures f_i and a matrix point at $\boldsymbol{x}$ is

$$\mathbb{E}\left[\sum_{i=1}^{N}\mathcal{F}_{f_i\leftrightarrow m}\middle|\boldsymbol{x}\right]. \tag{A1}$$

Applying Wald's equality, we have

$$\mathbb{E}\left[\sum_{i=1}^{N}\mathcal{F}_{f_i\leftrightarrow m}\middle|\boldsymbol{x}\right]=\mathbb{E}[N|\boldsymbol{x}]\mathbb{E}[\mathcal{F}_{f\leftrightarrow m}|\boldsymbol{x}]. \tag{A2}$$

Define the number density function $\lambda(\boldsymbol{x}',\boldsymbol{x})$ of fractures being centred at $\boldsymbol{x}'$ and intersecting matrix point $\boldsymbol{x}$ such that

$$\mathbb{E}[N|\boldsymbol{x}]=\int\lambda(\boldsymbol{x}',\boldsymbol{x})\,\mathrm{d}\boldsymbol{x}'. \tag{A3}$$

We define the conditional distribution

$$p(\boldsymbol{x}'\mid\boldsymbol{x})=\frac{\lambda(\boldsymbol{x}',\boldsymbol{x})}{\mathbb{E}[N\mid\boldsymbol{x}]},\quad\text{so that}\quad\int p(\boldsymbol{x}'\mid\boldsymbol{x})\,\mathrm{d}\boldsymbol{x}'=1. \tag{A4}$$

Then

$$\mathbb{E}[\mathcal{F}_{f\leftrightarrow m}|\boldsymbol{x}]=\int\mathbb{E}[\mathcal{F}_{f\leftrightarrow m}|\boldsymbol{x}',\boldsymbol{x}]p(\boldsymbol{x}'\mid\boldsymbol{x})\mathrm{d}\boldsymbol{x}'. \tag{A5}$$

Substituting this expression into (A2) yields

$$\mathbb{E}\left[\sum_{i=1}^{N}\mathcal{F}_{f_i\leftrightarrow m}\middle|\boldsymbol{x}\right]=\mathbb{E}[N\mid\boldsymbol{x}]\int\mathbb{E}[\mathcal{F}_{f\leftrightarrow m}|\boldsymbol{x}',\boldsymbol{x}]\frac{\lambda(\boldsymbol{x}',\boldsymbol{x})}{\mathbb{E}[N\mid\boldsymbol{x}]}\mathrm{d}\boldsymbol{x}'. \tag{A6}$$

Thus, the expected total fluid exchange is given by the spatial density of fractures multiplied by the expected fluid exchange per fracture:

$$\mathbb{E}\left[\sum_{i=1}^{N}\mathcal{F}_{f_i\leftrightarrow m}\middle|\boldsymbol{x}\right]=\int\lambda(\boldsymbol{x}',\boldsymbol{x})\mathbb{E}[\mathcal{F}_{f\leftrightarrow m}|\boldsymbol{x}',\boldsymbol{x}]\mathrm{d}\boldsymbol{x}'. \tag{A7}$$

Assuming

$$\mathbb{E}[\mathcal{F}_{f\leftrightarrow m}|\boldsymbol{x}',\boldsymbol{x}]=G(\mathbb{E}[p_f|\boldsymbol{x}']-\mathbb{E}[p_m|\boldsymbol{x}]) \tag{A8}$$

leads to

$$\mathbb{E}\left[\sum_{i=1}^{N}\mathcal{F}_{f_i\leftrightarrow m}\middle|\boldsymbol{x}\right]=\int\hat{g}(\boldsymbol{x}',\boldsymbol{x})(\mathbb{E}[p_f|\boldsymbol{x}']-\mathbb{E}[p_m|\boldsymbol{x}])\mathrm{d}\boldsymbol{x}' \tag{A9}$$

$$\text{with}\qquad\hat{g}(\boldsymbol{x}',\boldsymbol{x})=\lambda(\boldsymbol{x}',\boldsymbol{x})G, \tag{A10}$$

where the transfer coefficient G might depend on fracture and matrix permeability, fracture aperture, length and density, as studied in the previous works of the authors (Jenny 2020; Cao *et al.* 2025; Stalder *et al.* 2025).

Suppose the fractures have spatial number density (number of fractures per volume) $\rho_f(\boldsymbol{x})$ and joint probability density function of length and orientation $f_{L_f,\Theta_f}(l_f,\theta_f)$, then the number density function can be expressed as

$$\lambda(\boldsymbol{x}',\boldsymbol{x})=\int_{l_f>2|\boldsymbol{x}-\boldsymbol{x}'|}\rho_f(\boldsymbol{x}')\,f_{L_f,\Theta_f}(l_f,\theta_f=\theta_f(\boldsymbol{x},\boldsymbol{x}'))\,\mathrm{d}l_f, \tag{A11}$$

https://doi.org/10.1017/jfm.2026.11268 Published online by Cambridge University Press

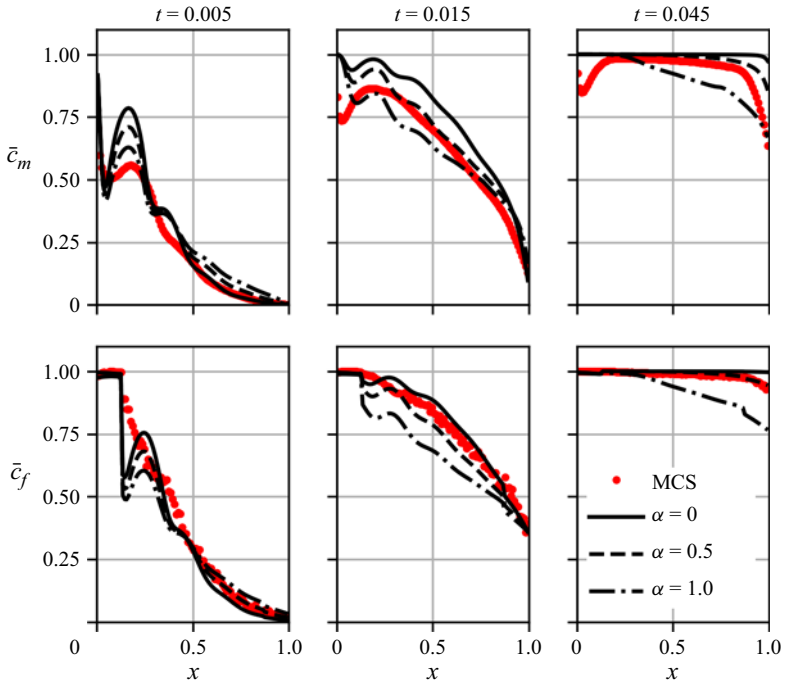


Figure 9. Sensitivity analysis of the constant α in (2.21) for test case 1. The three columns correspond to the three different times $t = 0.005$, $t = 0.015$ and $t = 0.045$ (left-, middle and right-hand columns, respectively). The black lines depict model predictions with different values of α and the red circles represent MCS reference data. Top row: matrix concentration; bottom row: fracture concentration.

where $\theta_f(\boldsymbol{x}, \boldsymbol{x}')$ denotes the inclination angle of the line connecting $\boldsymbol{x}$ and $\boldsymbol{x}'$.

Appendix B. Sensitivity analysis of the constant α

To investigate the sensitivity of the model to the constant α introduced in (2.21), we performed simulations for test case 1 with different values of α. Figure 9 shows the results for $\alpha = 0$, $\alpha = 0.5$ and $\alpha = 1.0$.

References

ARBOGAST, T, DOUGLAS, J.J. & HORNUNG, U. 1990 Derivation of the double porosity model of single phase flow via homogenization theory. *SIAM J. Math. Anal.* **21** (4), 823–836.

BEAR, J. 2013 *Dynamics of Fluids in Porous Media*. Courier Corporation.

BERKOWITZ, B., DROR, I., HANSEN, S.K. & SCHER, H. 2016 Measurements and models of reactive transport in geological media. *Rev. Geophys.* **54** (4), 930–986.

BERRE, I., DOSTER, F. & KEILEGAVLEN, E. 2019 Flow in fractured porous media: a review of conceptual models and discretization approaches. *Transp. Porous Med.* **130** (1), 215–236.

CACAS, M.C., LEDOUX, E., DE MARSILY, G., TILLIE, B., BARBREAU, A., DURAND, E., FEUGA, B. & PEAUDECERF, P. 1990 Modeling fracture flow with a stochastic discrete fracture network: calibration and validation: 1. The flow model. *Water Resour. Res.* **26** (3), 479–489.

CAO, S., STALDER, D., MEYER, D.W. & JENNY, P. 2025 Simulating flow in fractured porous media with spatially varying fracture statistics using a non-local kernel-based model. *J. Fluid Mech.* **1012**, A25 (in press).

HUNG, E.T., EFENDIEV, Y., LEUNG, W.T., VASILYEVA, M. & WANG, Y. 2018 Non-local multi-continua upscaling for flows in heterogeneous fractured media. *J. Comput. Phys.* **372**, 22–34.

DAGAN, G 1989 *Flow and Transport in Porous Formations*. Springer.

https://doi.org/10.1017/jfm.2026.11268 Published online by Cambridge University Press

DELGOSHAIE, A.H., MEYER, D.W., JENNY, P. & TCHELEPI, H.A. 2015 Non-local formulation for multiscale flow in porous media. *J. Hydrol.* **531**, 649–654.

DIETRICH, P., HELMIG, R., SAUTER, M., HÖTZL, H. & KÖNGETER, J. 2005 *Flow and Transport in Fractured Porous Media*. Springer-Verlag.

DURLOFSKY, L.J. 1991 Numerical calculation of equivalent grid block permeability tensors for heterogeneous porous media. *Water Resour. Res.* **27** (5), 699–708.

GEBAUER, S., NEUNHÄUSERER, L., KORNHUBER, R., OCHS, S., HINKELMANN, R. & HELMIG, R. 2002 Equidimensional modelling of flow and transport processes in fractured porous systems I. In *Developments in Water Science* (ed. S.M. Hassanizadeh, R.J. Schotting, W.G. Gray & G.F. Pinder), Computational Methods in Water Resources, vol. 47, pp. 335–342. Elsevier.

GEIGER, S., ROBERTS, S., MATTHÄI, S.K., ZOPPOU, C. & BURRI, A. 2004 Combining finite element and finite volume methods for efficient multiphase flow simulations in highly heterogeneous and structurally complex geologic media. *Geofluids* **4** (4), 284–299.

HYMAN, J.D., KARRA, S., MAKEDONSKA, N., GABLE, C.W., PAINTER, S.L. & VISWANATHAN, H.S. 2015 dfnWorks: a discrete fracture network framework for modeling subsurface flow and transport. *Comput. Geosci.* **84**, 10–19.

JENNY, P. 2020 Sub-representative elementary volume homogenization of flow in porous media with isolated embedded fractures. *J. Fluid Mech.* **901**, A20.

KASAP, E. & LAKE, L.W. 1990 Calculating the effective permeability tensor of a gridblock. *SPE Form. Eval.* **5** (02), 192–200.

LEE, S.H., LOUGH, M.F. & JENSEN, C.L. 2001 Hierarchical modeling of flow in naturally fractured formations with multiple length scales. *Water Resour. Res.* **37** (3), 443–455.

LI, X.S., DEMMEL, J.W., GILBERT, J.R., GRIGORI, L., SHAO, M. & YAMAZAKI, I. 1999 Superlu users' guide. *Tech. Rep.* LBNL-44289. Lawrence Berkeley National Laboratory. last update: June 2018.

MIN, K.B., JING, L. & STEPHANSSON, O. 2004 Determining the equivalent permeability tensor for fractured rock masses using a stochastic REV approach: method and application to the field data from Sellafield, UK. *Hydrogeol. J.* **12** (5), 497–510.

NEUMAN, S.P. 1988 Stochastic continuum representation of fractured rock permeability as an alternative to the REV and fracture network concepts. In *Groundwater Flow and Quality Modelling* (ed. E. Custodio, A. Gurgui & J.P. Lobo Ferreira), pp. 331–362. Springer Netherlands.

NEUNHÄUSERER, L., GEBAUER, S., OCHS, S., HINKELMANN, R., KORNHUBER, R. & HELMIG, R. 2002 Equidimensional modelling of flow and transport processes in fractured porous systems II. In *Developments in Water Science* (ed. S.M. Hassanizadeh, R.J. Schotting, W.G. Gray & G.F. Pinder), Computational Methods in Water Resources, vol. 47, pp. 343–350. Elsevier.

ODA, M. 1985 Permeability tensor for discontinuous rock masses. *Géotechnique* **35** (4), 483–495.

PALEOLOGOS, E.K. 2003 Stochastic methods for flow in porous media, coping with uncertainties. *EOS Trans. AGU* **84** (9), 84–84.

REICHENBERGER, V., JAKOBS, H., BASTIAN, P. & HELMIG, R. 2006 A mixed-dimensional finite volume method for two-phase flow in fractured porous media. *Adv. Water Resour.* **29** (7), 1020–1036.

SEN, M. & RAMOS, E. 2012 A spatially non-local model for flow in porous media. *Transp. Porous Med.* **92** (1), 29–39.

SNOW, D.T. 1965 *A Parallel Plate Model of Fractured Permeable Media*. University of California.

SNOW, D.T. 1969 Anisotropie permeability of fractured media. *Water Resour. Res.* **5** (6), 1273–1289.

STALDER, D., CAO, S., MEYER, D.W. & JENNY, P. 2025 Statistical integro-differential fracture model (Sid-FM) for isolated fractures with variable apertures and lengths. arXiv: 5027602.

https://doi.org/10.1017/jfm.2026.11268 Published online by Cambridge University Press